Synthesis and application of a ternary composite of clay, saw-dust and peanut husks in heavy metal adsorption

Henry H. Mungondori, Sandile Mtetwa, Lilian Tichagwa, David M. Katwire and Pardon Nyamukamba

ABSTRACT

The adsorption of a multi-component system of ferrous, chromium, copper, nickel and lead on single, binary and ternary composites was studied. The aim of the study was to investigate whether a ternary composite of clay, peanut husks (PH) and saw-dust (SD) exhibited a higher adsorption capacity than that of a binary system of clay and SD as well as a single component adsorbent of PH alone. The materials were used in their raw state without any chemical modifications. This was done to retain the cost effective aspect of the naturally occurring adsorbents. The adsorption capacities of the ternary composite for the heavy metals Fe^{2+}, Cr^{3+}, Cu^{2+}, Ni^{2+} and Pb^{2+} were 41.7 mg/g, 40.0 mg/g, 25.5 mg/g, 41.5 mg/g and 39.0 mg/g, respectively. It was found that the ternary composite exhibited excellent and enhanced adsorption capacity compared with both a binary and single adsorbent for the heavy metals Fe^{2+}, Ni^{2+} and Cr^{3+}. Characterization of the ternary composites was done using Fourier transform infrared spectroscopy (FTIR), X-ray diffraction (XRD) and thermogravimetric analysis (TGA). Kinetic models and adsorption isotherms were also studied. The pseudo second order kinetic model and the Langmuir adsorption isotherm best described the adsorption mechanisms for the ternary composite towards each of the heavy metal ions.

Key words | adsorption, heavy metals, lignocellulose, montmorillonite

Henry H. Mungondori (corresponding author)
David M. Katwire
Pardon Nyamukamba
Chemistry Department,
University of Fort Hare,
1 King Williams Town Road,
Alice 5700,
South Africa
E-mail: *henrymungondori@gmail.com*

Sandile Mtetwa
Chemistry Department,
University of Zimbabwe,
MP 167 Mt Pleasant,
Harare,
Zimbabwe

Lilian Tichagwa
Department of Polymer Technology and Engineering,
Harare Institute of Technology,
Ganges Road,
Belvedere,
Zimbabwe

INTRODUCTION

Water is essential to life. From the primeval age to date, one of the main conquests of humanity is the prevention of dehydration. In humans, water constitutes about 75% of the body content in infants and 55% in the elderly (Nicolaidis 1998). In this regard, the well-being of any human population depends on readily available clean water. As the world became more industrialized, water bodies, especially the natural ones, have been under attack by pollutants. Heavy metals, a constituent of inorganic water pollutants, are of major concern due to the health risks they pose to humans and other species if accumulated. The elements are naturally occurring and commonly found even in biological processes; however they need to be contained within certain concentration limits, as they become toxic above stipulated levels. Exposure to heavy metals continues to increase in many parts of the world, especially in underdeveloped countries (Berglund *et al.* 2001). Some of the main heavy metals that have adverse health effects are Cr^{3+}, Pb^{2+} and Cu^{2+}. A recent case of heavy metal pollution in water is the Flint Water Crisis of Michigan in the USA. The residents of the area consumed water from the Flint river, which was heavily polluted by lead. The residents who had been drinking the water suffered lead poisoning (Moore 2016). Indeed, the effects of heavy metal pollution in water bodies prove to be fatal.

For decades certain processes have been employed for the removal of heavy metals in water. The popular conventional ways include chemical precipitation, flotation, adsorption, ion-exchange and electrochemical deposition (Wang *et al.* 2008). However, these conventional methods have proved to be disadvantageous in that they are overall not environmentally friendly and are costly. The adsorption method has gained much interest over the years. Adsorption involves the uptake of contaminants and consists of several mechanisms such as surface adsorption, partition, surface precipitation as well as structural incorporation (Malamis & Katsou 2013; Yuan *et al.* 2013). Various improved methods have been devised to produce cost-effective and more

doi: 10.2166/wst.2017.123

environmentally friendly adsorbents. As the years progressed, more improved mechanisms of adsorption have been researched, with the use of nanotechnology being a major source of the improved efficiency of adsorbents.

Nano-based materials such as nanostructures, nanotubes and hollow nanospheres have been widely researched and applied in the removal of heavy metal ions in water. Notable work includes the preparation and use of bismuth hollow nanospheres that exhibited a high capacity for Cr(IV) removal. The main advantage of these nanospheres is that they are prepared via a facile solvothermal method and are employable over a large pH range (2–11) (Qin *et al.* 2012a, 2012b). ą-Fe_2O_3 nanostructures have also been looked into in the removal of Cr(IV) ions. Also prepared via a facile hydrothermal method, the nanostructures exhibited high Cr(IV) adsorption capacity and the prepared nanorods had a large surface area and the ideal pore distribution for efficient ion uptake (Liu *et al.* 2014). BiOBr nanostructures have also been synthesized via a facile, fast microwave irradiation and self-assembly method. The nanostructures had large surface area, as evidenced by Brunauer–Emmett–Teller (BET) surface area analysis; hence, their Cr(VI) removal capacity was excellent (Li *et al.* 2012). Also, BiOX (X = Cl, Br, I) nanostructures have been shown to demonstrate excellent Cr(VI) adsorption. These nanostructures in flower-like shape exhibit high BET surface area as well as a large band gap. Through a facile and rapid microwave irradiation method in mannitol solution, the BiOX nanostructures are synthesized, with their morphology and size easily manipulated by key variables (Li *et al.* 2013). An attractive approach to the use of nanostructures in heavy metal adsorption is the absence of certain additives such as templates or surfactants. As demonstrated by Qin *et al.* (2012a, 2012b), Bi_2O_3 as well as $(BiO)_2$ CO_3 nanotubes exhibit a highly remarkable adsorption capacity, i.e. 79 mg g^{-1} for Cr(IV) when synthesized by a facile solvothermal method.

Recent investigations have given insight into the use of biosorbents as well as naturally occurring adsorbents with little/no chemical modification as the futuristic technology in heavy metal removal (Akopmie *et al.* 2015; Klapiszewski *et al.* 2015; Zhang & Wang 2015). There is minimal literature available on the use of three naturally occurring adsorbents which when combined, form a ternary composite that has enhanced adsorption capacity compared with either a binary composite or a single component. Hence, the aim of this research was to study the adsorption properties of a ternary composite and compare them with those of a binary composite as well as a single adsorbent. The materials of interest were montmorillonite (MMT), and the lignocellulosic materials: saw-dust (SD) and peanut husks (PH).

MMT is a naturally occurring layered, crystalline 2:1 phyllosilicate clay. Its crystal lattice is comprised of octahedral alumina that is fused between two silica sheets that are tetrahedral. Thus the name 2:1, meaning 2 tetrahedral Si sheets: 1 octahedral Al sheet. The layers in MMT are negatively charged due to the isomorphic substitution by either Mg^{2+} or Al^{3+} in the octahedral or tetrahedral layers. This negative charge is, however, balanced by cations in the interlayers, and these cations are exchangeable (Alexandre & Dubois 2000). MMT adsorbs heavy metals mainly by two mechanisms, which are: cation exchange in the interlayer from interaction between ions and negative permanent charge, and also by the formation of inner-sphere complexes through Si-O- and Al-O- groups present on the edges of the clay (Abollino *et al.* 2003).

Lignocellulosic waste biomasses are growing to be a valuable resource worldwide in their application in heavy metal removal by serving as an alternative to expensive ion-exchange resins (Lopiĉić *et al.* 2016). Lignocellulose materials mainly consist of cellulose, hemicellulose as well as lignin. These polymers are organized in three-dimensional matrices of plant walls that are rich in functional groups such as –COOH and –OH, which readily bind to cations (Torab-Mostaedi *et al.* 2013).

When clay and a polymer are mixed together, the resulting composite can take up one of the following morphologies: (i) intercalated; (ii) exfoliated; (iii) flocculated; and (iv) non-mixed. These morphologies are highly dependent on the interphase forces between the polymer and the clay. Intercalation is where a polymer is inserted into a silica structure and the insertion is crystallographically regular, whereas exfoliation is when individual clay layers randomly separate in a continuous polymer matrix. The interlayer spacing between the MMT sheets depends on the charge of the clay. Flocculated composites are similar to intercalated structure; however, flocs form due to interaction between OH– groups of silicate (Zaarei *et al.* 2008). Kumar *et al.* (2011) researched the application of cellulose-clay biosorbent in removal of chromium from industrial water. The researchers found that the maximum adsorption capacity of the biosorbent to chromium was 22.2 mg/g and the adsorption mechanism was best explained by the Langmuir isotherm model. Wysokowski *et al.* (2014) and Klapiszewski *et al.* (2015) recently reported that the combination of two or more naturally occurring components such as silica/bentonite together with green polymers such as lignin to produce highly efficient material that combines favorable properties of both precursors can be achieved.

MATERIALS AND METHODS

Materials

PH, SD and MMT clay were all procured at Mbare Msika in Harare Zimbabwe. The heavy metal ions stock solutions were prepared from the following salts: $Fe(SO_4{\cdot}7H_2O)$ (99%, Skylab Chemicals), $Pb(NO_3)_2$ (99%, Skylab Chemicals), $CrCl_3{\cdot}6H_2O$ (96%, Sigma Aldrich), $Ni(NO_3)_2{\cdot}6H_2O$ (99%, Skylab Chemicals), $Cu(SO_4)$ (99%, Skylab Chemicals), absolute ethanol (99%, Skylab Chemicals) and deionized water.

Synthesis of binary and ternary composites

The MMT, SD and PH were pulverized to powder form. The binary composites were composed of MMT and SD weighed in different ratios as shown in Table 1. The ternary composites were composed of MMT, SD and PH weighed in different ratios as shown in Table 1.

Each sample was mixed in a 200 mL solution containing a 1:1 ratio of ethanol and deionized water. The mixture was stirred at 25 °C on a magnetic stirrer for 1 hour. The excess solvent was decanted and the remaining mixture centrifuged for 10 minutes at 1,000 rpm. The supernatant fluid was decanted and the residue dried in an oven for 15 hours at 50 °C.

Adsorption studies (batch equilibrium process)

A 0.025 g sample of each composite was added to 100 mL (10 ppm) solutions containing Ni^{2+}, Pb^{2+}, Cu^{2+}, Cr^{3+} and Fe^{2+}. The pH of each mixture was maintained between pH 6 and 7 and the temperature was kept at room temperature. Each solution was shaken on a mechanical shaker for 1 hour. The solutions were analyzed post adsorption on a flame atomic absorption spectrometer.

Table 1 | Molar ratios by mass of MMT: SD: PH

Ternary composite				Binary composite		
Sample ID	MMT/g	SD/g	PH/g	Sample I.D	MMT/g	SD/g
S1	9.0	0.5	0.5	M1	9.0	1.0
S2	8.0	1.0	1.0	M2	8.0	2.0
S3	7.0	1.5	1.5	M3	7.0	3.0
S4	6.0	2.0	2.0	M4	6.0	4.0
S5	5.0	2.5	2.5	M5	5.0	5.0
S6	4.0	3.0	3.0	M6	4.0	6.0
S7	3.0	3.5	3.5	M7	3.0	7.0
S8	2.0	4.0	4.0	M8	2.0	8.0
S9	1.0	4.5	4.5	M9	1.0	9.0

Kinetic model studies

The best adsorbent from the ternary composite was chosen. A 0.025 g sample of the adsorbent was added to a 100 mL (10 ppm) solution containing Ni^{2+}, Pb^{2+}, Cu^{2+}, Cr^{3+} and Fe^{2+}. The total contact time for shaking on the mechanical shaker was 6 hours, aliquots being withdrawn every 30 minutes. The pH was maintained between 6 and 7 and the temperature was kept at 25 °C during the adsorption process. The 12 samples were analyzed post adsorption on a flame atomic absorption spectrometer.

Adsorption isotherm studies

The best adsorbent from the ternary composite batch was chosen. A 0.025 g sample of the adsorbent was added to 100 mL solutions containing different concentrations of 4.5 ppm, 6.0 ppm, 7.5 ppm, 9.0 ppm, 10.5 ppm, 12.0 ppm, 13.5 ppm and 15.0 ppm of Ni^{2+}, Pb^{2+}, Fe^{2+}, Cr^{3+} and Cu^{2+}. The contact time for each sample on the mechanical shaker was 4 hours. The pH was maintained between 6 and 7 and the temperature was kept at 25 °C during the adsorption process. The eight samples were analyzed post-adsorption on a flame atomic absorption spectrometer.

Characterization

The characterization was carried out on all the synthesized ternary composite samples, binary composite, M4, and MMT. Fourier transform infrared spectra (FTIR) were recorded in the frequency range of 4,000–400 cm^{-1} using a Bruker FTIR spectrometer, Model Tensor 27 (Ettlingen, Germany). The X-ray diffraction (XRD) scans were recorded in the 2θ range of 0–15 ° on a Bruker AXS D8 Advance X-ray diffractometer. Thermo-gravimetric analysis (TGA) curve was recorded in the temperature range of 0–1,000 °C using a Perkin Elmer TGA 7 Thermo-gravimetric Analyzer. BET surface area analysis for nitrogen adsorption/desorption data was carried out at liquid nitrogen temperature on a Tristar II 3,020 V1.02 surface area and pore size analyzer.

RESULTS AND DISCUSSION

FTIR, TGA, XRD and BET analyses

Fourier transform infrared

The FTIR spectra for all the synthesized ternary composites are shown in Figure 1. Sample 1, with MMT:SD:PH ratio of 9:0.5:0.5 by mass, has a sharp strong peak at 3,621 cm^{-1}, which is associated with the stretching of hydroxyl groups that are coordinated to octahedral cations, especially the Al^{3+} (Ezquerro *et al.* 2015). A broad stretch at 3,386 cm^{-1} is characteristic of the –OH stretch of water in the interlayer region with H bonding. This bond correlates with the low intense stretch at 1,641 cm^{-1}, which is caused by the bending vibration mode of adsorbed water (Frost & Rintoul 1996). The low frequency region has the most intense bands at 1,114 cm^{-1} and 1,002 cm^{-1} associated with Si–O stretching, out-of plane for the former and in-plane for the latter. Metal-metal OH bonds are shown at the 911 cm^{-1} sharp band, for Al-AlOH bending, and the last stretch between 749 and 682 cm^{-1} is likely due to the presence of quartz in the sample (Tyagi *et al.* 2006). Some of the bands are characteristic of lignocellulose. A typical lignin based peak occurs at 1,506 cm^{-1} as a sharp band characteristic of the aromatic skeletal vibrations (Sun *et al.* 2005). The stretch at 1,268 cm^{-1} is a band caused by the C–O stretching in the ring, aromatic C–H in-plane deformations as well as aromatic C–H out-of plane bending vibrations. The C–O bonds in unconjugated ketones are shown at 732 cm^{-1} together with carbonyls and carboxylic acids (Jahan & Mun 2007) from the bonding between groups of the lignocellulose and MMT. All the synthesized composites contain the same materials, i.e. MMT and lignocellulose, with, however, a difference in the molar ratios by mass. Hence, they are expected to have the same functional groups' bands observed in the FTIR spectra as shown in Figure 1. The difference is in the intensity of the bands, as some composites contain a higher lignocellulose or MMT content than others.

X-ray diffraction

The basal peak for MMT occurs at about 5.98 °–6.98 ° with a d-spacing ranging between 12.3 and 14.6 Å. If intercalation takes place, the 2θ angle is expected to shift to a lower angle (i.e. less than the 5.98 ° and 6.98 ° range) due to pushing apart of the clay layers by the guest molecule, thereby increasing the d-spacing between layers. Also, the peak between 5.98 °–6.98 ° is expected to disappear to show the disruption of the crystalline structure of the clay material as the guest molecule inserts itself between the layers, thus causing them to collapse (Zhang & Wang 2015). From the XRD spectra shown in Figure 2, it is observed that the basal peak for MMT alone is no longer present in all the ternary composites (Samples 1–8). This can be attributed to the

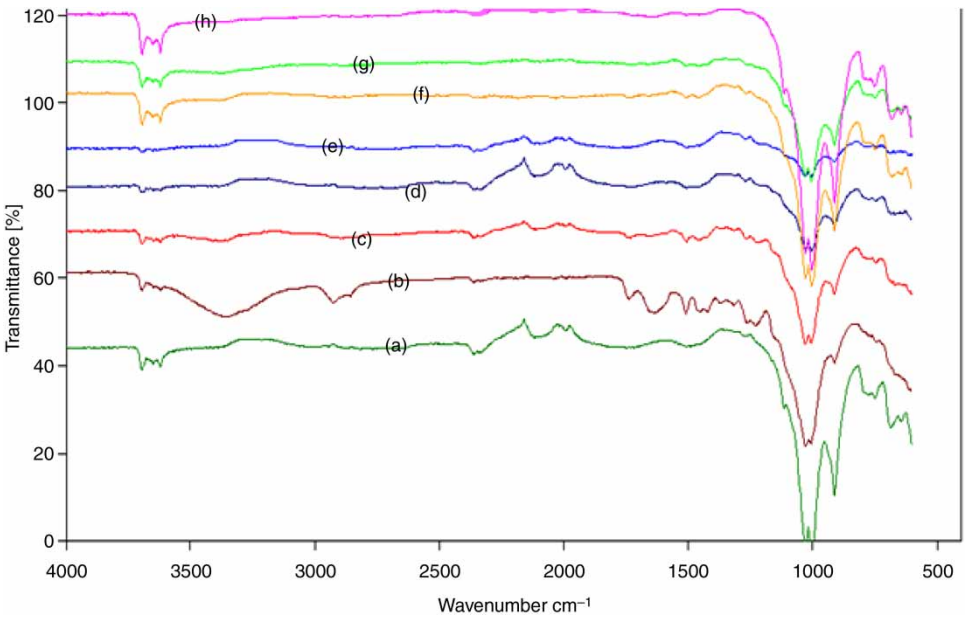

Figure 1 | FTIR spectra for (a) MMT:SD:PH (9:0.5:0.5), (b) MMT:SD:PH (8:2:2), (c) MMT:SD:PH (7:1.5:1.5), (d) MMT:SD:PH (6:2:2), (e) MMT:SD:PH (5:2.5:2.5), (f) MMT:SD:PH (4:3:3), (g) MMT:SD:PH (3:3.5:3.5), (h) MMT:SD:PH (2:4:4).

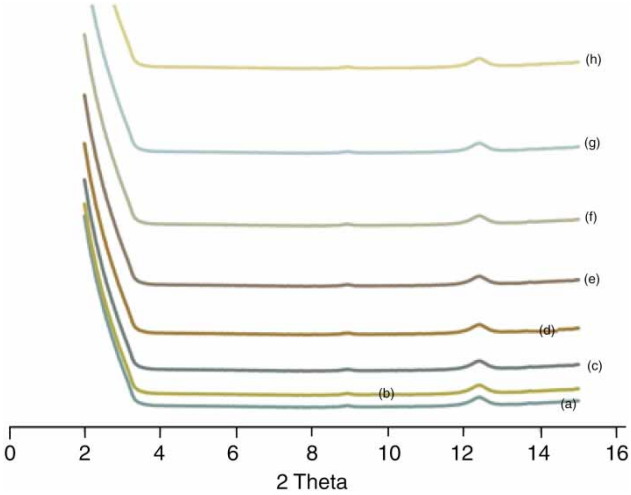

Figure 2 | XRD scan for (a) MMT:SD:PH (9:0.5:0.5), (b) MMT:SD:PH (8:2:2), (c) MMT:SD:PH (7:1.5:1.5), (d) MMT:SD:PH (6:2:2), (e) MMT:SD:PH (5:2.5:2.5), (f) MMT:SD:PH (4:3:3), (g) MMT:SD:PH (3:3.5:3.5), (h) MMT:SD:PH (2:4:4), (g) MMT:SD:PH (1:4.5:4.5), (h) MMT:SD:PH (2:4:4).

fact that the crystalline structure of the MMT was disrupted as the lignocellulose polymer intercalated itself between the weakly held interlayers. This suggests that the composite has an intercalated-flocculated structure**.** An investigation was carried out by Franco & Ruiz Cruz (2004) studying the factors that influence the degree of intercalation of a silicate based material, kaolin, which belongs to the same family as MMT. The experiments showed that intercalation was dependent on particle size, degree of ordering, type of guest molecules, method of intercalation and the presence of impurities. In light of this, the increase of the 2θ angle may be attributed to one of these factors.

Thermogravimetric analysis

With reference to the derivative thermogram (DTG) plot in Figure 3, information on the different steps of the decomposition of the MMT as well as the pyrolysis of lignin is obtained. It can be seen that all the ternary composites (samples 1–9) have characteristic peaks at the region below 100 °C, roughly ranging from 50 °C to 80 °C. At this stage the moisture absorbed by lignin evaporates and there is desorption of water and physisorbed species such as N_2 or CO_2 (Ezquerro *et al.* 2015). The region between 320 and 380 °C is shown for the ternary composites (samples 1–9), and at this stage the heat begins to pyrolyze the lignin and the fragmentation of its side chains begins to occur. There occurs decarboxylation as well as decarbonylation, which allow the polymer to decompose into its constituent groups (CO, CO_2, CH_4, CH_3COOH and HCOOH) (Maschio *et al.* 1992). This peak is also characterized by a major weight loss of ≈ 99%. This is due to the fact that most of the organic content that constitutes the material is decomposed. Also, at this temperature decomposition of MMT organic species occurs. It is observed that there are materials that decompose at a lower temperature (320 °C)

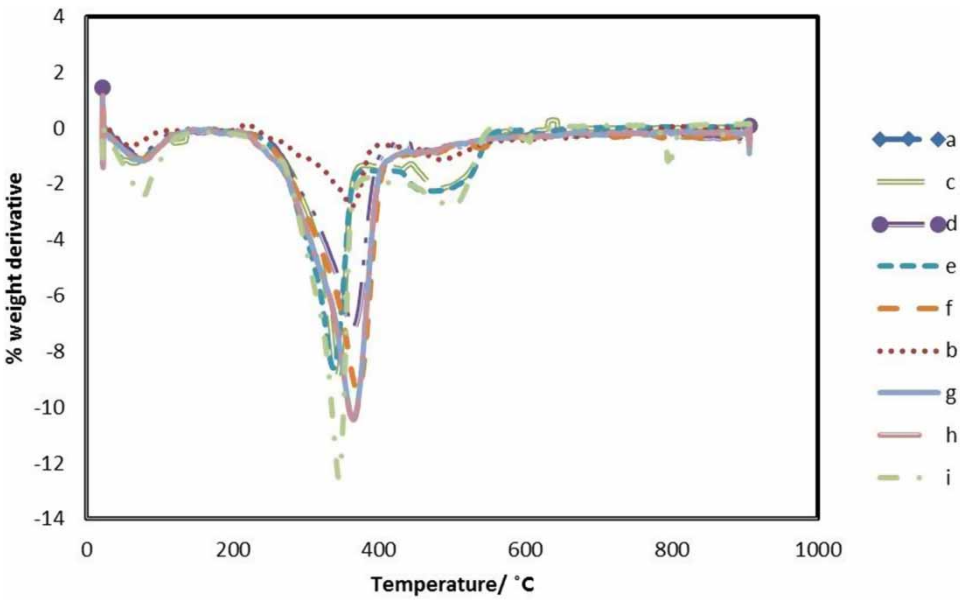

Figure 3 | DTG curve for (a) MMT:SD:PH (9:0.5:0.5), (b) MMT:SD:PH (8:1:1), (c) MMT:SD:PH (7:1.5:1.5), (d) MMT:SD:PH (6:2:2), (e) MMT:SD:PH (5:2.5:2.5), (f) MMT:SD:PH (4:3:3), (g) MMT:SD:PH (3:3.5:3.5), (h) MMT:SD:PH (2:4:4), (i) MMT:SD:PH (1:4.5:4.5).

and those that do so at higher temperatures (360–380 °C); the former are less thermally stable than the latter. The last peak, between 450 and 500 °C, is characterized by not much weight loss. In this region there occurs the dehydroxylation of the aluminosilicate layers of the MMT (Ezquerro *et al.* 2015). After this stage there is not much weight loss, meaning the decomposition process is slowed down. The registered weight still present is >1%. This is likely due to the salts formed during precipitation. It can also be attributed to products associated with organic carbonaceous residue (Xi *et al.* 2007).

BET

The BET surface areas of MMT, S2 and M4 are shown in Table 2. As expected, the surface areas of both composites, M4 at 12.93 $m^2 g^{-1}$ and S2 at 16.71 $m^2 g^{-1}$, are much lower than that of MMT alone at 28.58 $m^2 g^{-1}$. This is due to the filling up of the pores of MMT by lignocellulosic materials: PH and/or SD. As filling up occurs, porosity decreases; hence, nitrogen adsorption decreases as well to yield lower surface area (Koc *et al.* 2014). The binary and ternary composites, M4 and S2 respectively, differed in their surface areas. This is because the binary composite, M4, had a higher loading of lignocellulose (SD) in the MMT than S2. Hence, more of the MMT pores in M4 were filled up by the SD, resulting in it exhibiting a lower surface area.

Batch adsorption studies

The percentage removal capacity on the single component adsorbents, i.e. MMT, SD and PH alone, for each heavy metal cation was first analyzed. This is shown in Figure 4. It was concluded that the PH (N3) exhibited the highest percentage removal of all three single adsorbents.

A batch equilibrium process was done so as to determine which of the prepared samples from the ternary and binary composite batch exhibited the best and most plausible percentage removal capacity of the heavy metal cations. The ternary composite batch had sample S2 (out of the nine samples) with a MMT: SD: PH ratio of 8:1:1 by mass as its best adsorbent. The binary composite batch had sample M4 (out of the nine samples) with an MMT: SD ratio of 6:4 by mass as its best adsorbent. A comparison of the three adsorbents, as representatives of the ternary, binary and single component batches, is shown in Figure 5. The graph shows a gradual enhancement of the percentage removal from the single component to the ternary composite for the metals Fe^{2+}, Cr^{3+} and Ni^{2+}. A synergistic effect is seen to occur here, as the combination of the three adsorbents resulted in higher metal ion uptake as compared with the single component adsorbents alone. This can be attributed to the fact that as the number of adsorbents increased, the number of binding sites where the metals can interact increased as well, and more of the metal ions in aqueous solution could be removed. It should be noted, however, that Cr^{3+} exhibited complete removal by both the binary composite and the ternary composite. The pH was maintained at

Table 2 | BET surface areas and pore volumes

Material	Surface area/$m^2 g^{-1}$	Pore volume/$cm^3 g^{-1}$
MMT	28.58	0.113
M4 (binary composite)	12.93	0.0657
S2 (ternary composite)	16.71	0.0884

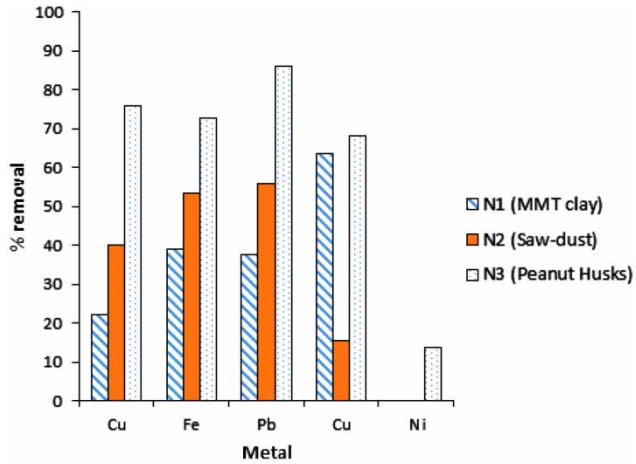

Figure 4 | Trend analysis of each single component adsorbent.

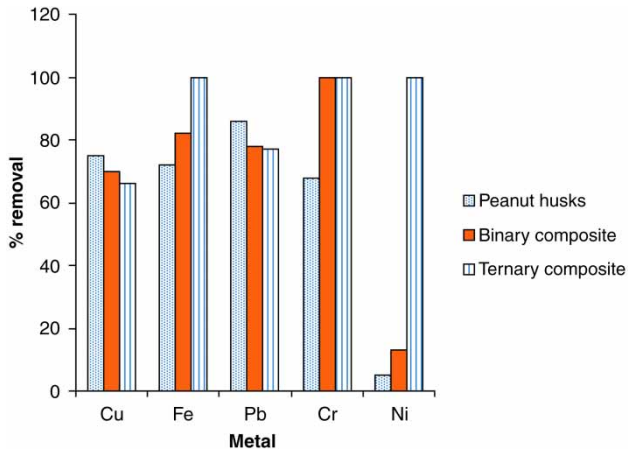

Figure 5 | Trend analysis of ternary, binary and single component adsorbents.

6–7 in the batch adsorption studies and as previously observed by (Lukman *et al.* 2013), Cr^{3+} is adsorbed best at pH 6. This suggests that the adsorption of Cr was well suited to the pH conditions; hence, it was the most preferred in binding amongst all the other metals, and its interaction with the adsorbent was not as much related to the number of available binding sites. The percentage removal trend decreases from the single component to the ternary composite for Cu^{2+} and Pb^{2+}. This phenomenon may be due to the fact that Pb^{2+} and Cu^{2+} uptake is more related to the lignocellulose groups, such as the COOH and N-H, where chelation and/or ion exchange can take place. The amount of lignocellulose in the composite (by mass) increased from the ternary composite to the single component. Thus, Pb^{2+} and Cu^{2+} adsorption was higher in the single component than in both the ternary and binary composites, a result that concludes the lack of synergistic effect contribution to metal ion uptake for these particular ions. The adsorption of Ni^{2+} was very poor for the single component adsorbent, which may be due to a previous finding by Nachtegaal *et al.* (2005), who reported that Ni^{2+} is known to undergo structural incorporation into the vacant sites of the composite, meaning its adsorption would be more favored to an adsorbent that has more MMT, which has vacant sites other than the lignocellulose component.

Effect of contact time

Figure 6 shows the effect of varying adsorption time on the adsorption process. It can be seen that the rate of adsorption increased in the initial stages of the contact time. However, a saturation point was reached at an average of 220 minutes for each of the metal ions. At this point, it is believed that the adsorption sites were all saturated by heavy metal cations and could no longer bind to any more cations even when the contact time was increased. This saturation point can be termed 'the adsorption capacity at equilibrium (q_e)', which was calculated as 22.89 mg/g, 38.4 mg/g, 35.23 mg/g, 37.94 mg/g and 36.34 mg/g for Cu^{2+}, Fe^{2+}, Pb^{2+}, Cr^{3+} and Ni^{2+}, respectively.

Kinetic models

To obtain kinetic models, both the adsorption times at equilibrium and the concentration of heavy metal cations at equilibrium for each of the metal ions were chosen for the calculations. Various equations were used to describe the kinetic models followed by an adsorption process. The simplest ones, which were analyzed, were the pseudo-first order and pseudo-second order rate equations.

Pseudo-first order adsorption kinetic model

The pseudo-first order equation was given by Lagergren as a possible mechanism for the solid/liquid adsorption systems. It can be expressed in either the non-linear form as:

$$q_t = q_e(1 - e^{-k1t}) \tag{1}$$

or the linear form as

$$\log(q_e - q_t) = \log\left(q_e - \frac{k_1 t}{2.303}\right) \tag{2}$$

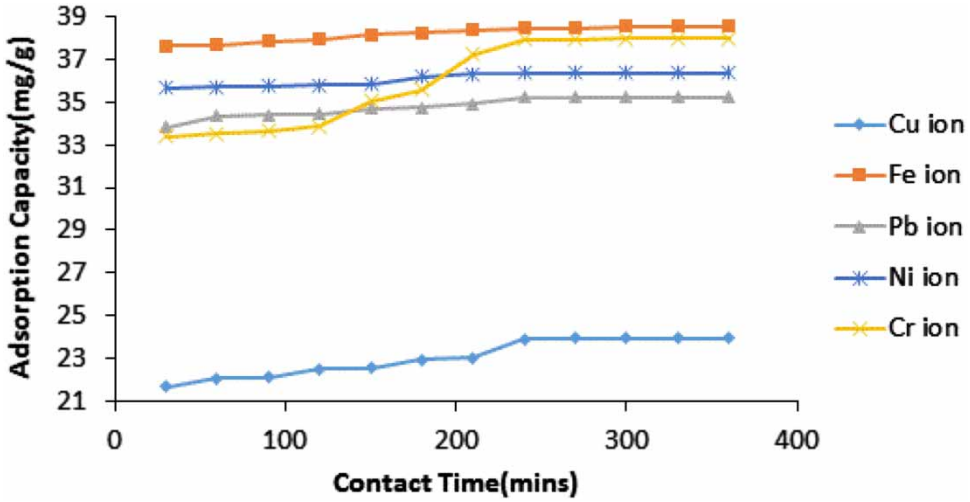

Figure 6 | Effect of contact time on adsorption for ternary composite.

In this research, the linear form was used to describe the pseudo rate order equation, where

q_e: adsorption capacity at equilibrium
q_t: adsorption capacity at time (t)
k_1: pseudo-first order rate constant (determined experimentally from data plot)

A linear plot of $\log(q_e - q_t)$ vs t is shown in Figure 7.

Pseudo-second order adsorption kinetic model

The pseudo-second order model is popularly known as Ho's model. There are five different linear forms of Ho's model (Kumar 2006) and (Zhou *et al.* 2016), and in this research type 1 was utilized. The formula

$$\frac{t}{q_t} = \frac{1}{k_2 qe^2} + \frac{t}{q_e} \tag{3}$$

is used to describe the pseudo-second order rate equation. k_2 is the pseudo-second order rate constant, which is determined from the plot of experimental data. A linear plot of (t/q_t) vs t is shown in Figure 8.

The correlation coefficients (R^2 values) for the pseudo-first and pseudo-second order plots are shown in Table 3.

It can be observed that each metal ion type has a higher R^2 value for the pseudo second order model, where the plot of (t/q) vs t exhibits high linearity. Therefore, it can be safely concluded that the kinetic model that best fits the adsorption mechanism for all ions is the pseudo-second order model. This means that the adsorption rate of the heavy metal ions is dependent on the concentration of the ions that are already present on the surface of the adsorbent, as well as the amount adsorbed at equilibrium.

Effect of initial heavy metal ion concentration

A plot of adsorption capacity (q) versus initial heavy metal concentration is shown in Figure 9 for each of the cations Fe^{2+}, Ni^{2+}, Cu^{2+}, Pb^{2+} and Cr^{3+}. It can be seen that for low metal cation concentrations, i.e. between 4.5 ppm and 6.0 ppm, the uptake increased greatly. These are the initial stages of adsorption; hence, it is expected that the number of available adsorption sites is plenty with respect to the small amount of ions present in solution. At about

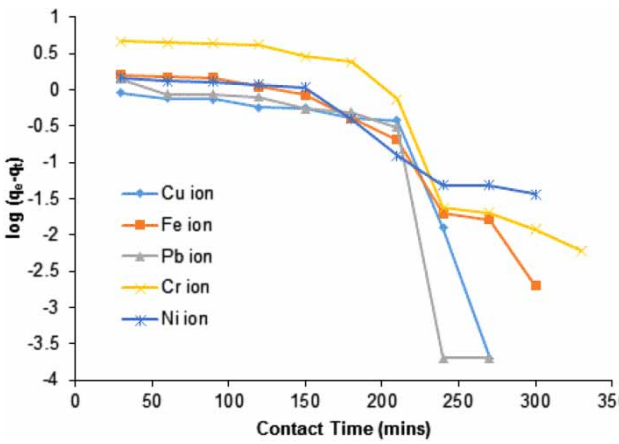

Figure 7 | Pseudo-first order adsorption kinetic model.

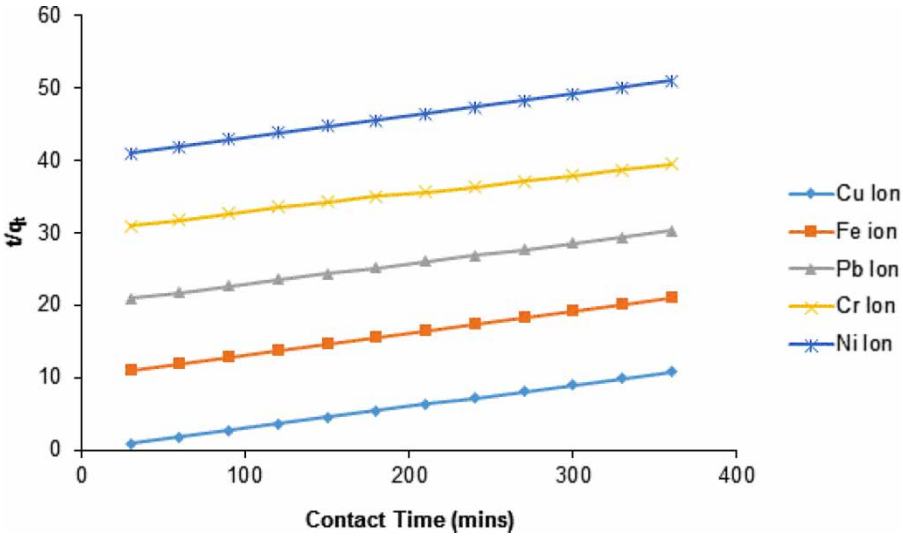

Figure 8 | Pseudo-second order adsorption kinetic model.

Table 3 | Correlation coefficients of pseudo-first and pseudo-second order kinetic models

Metal ion type	Pseudo-first order model (R^2 value)	Pseudo-second order model (R^2 value)
Cu^{2+}	0.843	0.999
Fe^{2+}	0.849	0.999
Pb^{2+}	0.636	0.999
Cr^{3+}	0.843	0.998
Ni^{2+}	0.883	0.999

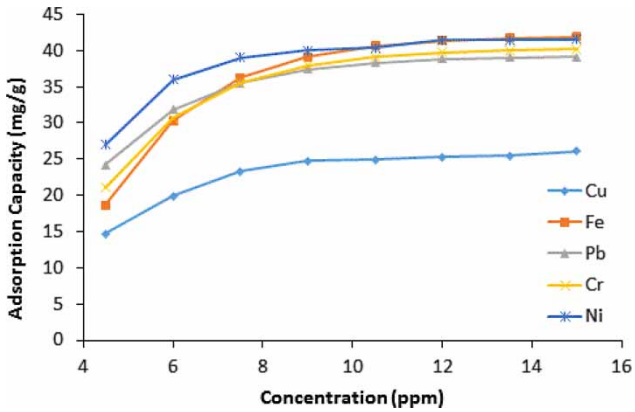

Figure 9 | Effect of initial heavy metal ion concentration on adsorption for ternary composite.

13.5 ppm, the adsorption process is seen to become steady for the metal ions. At this point, the amount of heavy metal ions in solution is about three times higher than that present in the initial stages; hence, it is expected that a saturation point has been reached. Thus, it can be concluded that further increase in heavy metal concentration slows down the adsorption process. The process is very efficient only up to a metal concentration of 13.5 ppm.

Adsorption isotherms

To obtain adsorption isotherms, the adsorption capacity at equilibrium should be calculated. The amount of heavy metal adsorbed at equilibrium q_e is given by the formula:

$$q_e = \left(\frac{C_o - C_e}{m}\right)v \tag{4}$$

where C_o: initial heavy metal concentration, C_e: heavy metal concentration at equilibrium, m: mass of adsorbent used, v: volume of heavy metal ion solution.

Langmuir adsorption isotherm

The principle of a Langmuir model is that 'an adsorbent has a fixed number of available binding sites', i.e. a limited adsorption capacity. These sites are all identical and each of the sites can only bind one molecule. This can be referred to as 'monolayer adsorption'. The Langmuir equation is shown as:

$$\frac{C_e}{q_e} = \frac{1}{bq_m} + \frac{C_e}{q_m} \tag{5}$$

where q_m and b are Langmuir isotherm coefficients and q_m represents the maximum adsorption capacity. A plot of (C_e/q_e) vs C_e was drawn to observe linearity, and it's shown in Figure 10.

Freundlich adsorption isotherm

In the Freundlich model, multilayer adsorption is assumed to take place. There possibly occurs the uptake of the solute onto different adsorption classes on each site present on the adsorbent. The Freundlich equation is given by:

$$q_e = K_f C_e^{(1/n)} \tag{6}$$

where K_f and n are Freundlich constants. A linear plot of $\log q_e$ vs C_e is shown in Figure 11.

The correlation coefficients (R^2 values) for the Langmuir and Freundlich plots are shown in Table 4.

It can be observed that each metal ion has a higher value of R^2 for the Langmuir model than for the Freundlich model. In this regard, it can be concluded that the Langmuir adsorption isotherm best fits the adsorption mechanism of the adsorbate to the adsorbent.

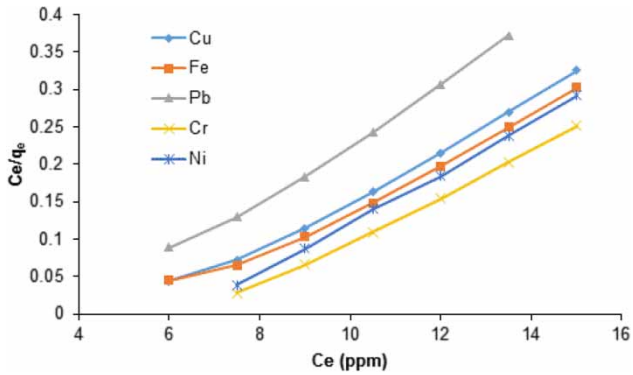

Figure 10 | Langmuir adsorption isotherm plot.

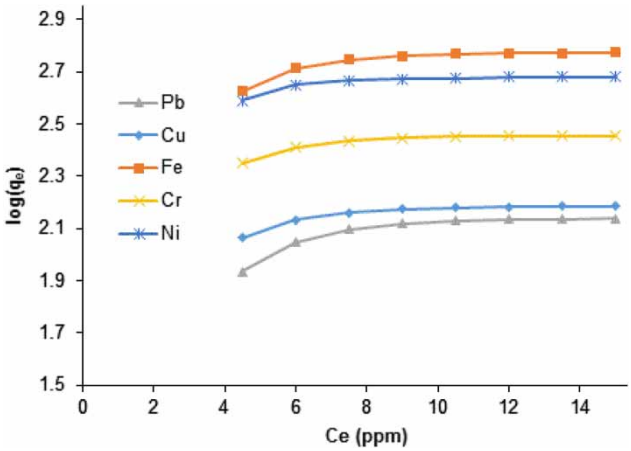

Figure 11 | Freundlich adsorption isotherm plot.

Table 4 | Correlation coefficients for Langmuir and Freundlich adsorption isotherms

Metal ion type	Langmuir model (R^2 value)	Freundlich model (R^2 value)
Cu^{2+}	0.991	0.669
Fe^{2+}	0.986	0.658
Pb^{2+}	0.994	0.679
Cr^{3+}	0.992	0.676
Ni^{2+}	0.998	0.608

CONCLUSION

The ternary composite exhibited enhanced adsorption capacity for the metals Fe^{2+}, Ni^{2+}, Cr^{3+} compared with the single and binary composites. The adsorption capacities were 41.7 mg/g, 41.5 mg/g, and 40.0 mg/g for the metals, respectively. The single component adsorbent of PH exhibited enhanced adsorption capacity for the metals Pb^{2+} and Cu^{2+} compared with the binary and ternary composites. The adsorption capacity for each metal was 45.8 mg/g and 30.2 mg/g, respectively. The ternary composite followed the Langmuir adsorption isotherm for each metal ion and the pseudo-second order kinetic model. The adsorbents exhibited excellent adsorption properties and should be considered for use on a large scale in industry.

REFERENCES

Abollino, O., Aceto, M., Malandrino, M., Sarzanini, C. & Mentasti, E. 2003 Adsorption of heavy metals on Na-montmorillonite, effect of pH and organic substances. *Water Research* **37**, 1619–1627.

Akpomie, K., Folasegun, A. & Kayode, O. 2015 Mechanism on the sorption of heavy metals from binary-solution by a low cost montmorillonite and its desorption potential. *Alexandria Engineering Journal* **54** (3), 757–767.

Alexandre, M. & Dubois, P. 2000 Polymer-layered silicate nanocomposites: preparation, properties and uses of a new class of materials. *Materials Science and Engineering* **28**, 1–63.

Berglund, M., Elinder, C. & Järup, L. 2001 *Humans Exposure Assessment: An Introduction.* World Health Organization, Stockholm, Sweden, pp. 20–21.

Ezquerro, C., Ric, G., Miñana, C. & Bermejo, J. 2015 Characterization of montmorillonites modified with organic divalent phosphonium cations. *Applied Clay Science* **111**, 1–9.

Franco, F. & Ruiz Cruz, M. 2004 Factors influencing the intercalation degree ('reactivity') of kaolin minerals with potassium acetate, formamide, dimethylsulphoxide and hydrazine. *Clay Minerals* **39** (2), 193–205.

Frost, R. & Rintoul, L. 1996 Lattice vibrations of montmorillonite: an FT Raman and X-ray diffraction study. *Applied Clay Science* **11**, 171–183.

Jahan, M. & Mun, S. 2007 Characteristics of dioxane lignins isolated at different ages of Nalita wood (*Trema orientalis*). *Journal of Wood Chemistry and Technology* **27**, 83–98.

Klapiszewski, L., Bartczak, P., Wysokowski, M., Jankowska, M., Kabat, K. & Jesionowski, T. 2015 Silica conjugated with kraft lignin and its use as a novel 'green' sorbent for hazardous metal ions removal. *Chemical Engineering Journal* **260**, 684–693.

Koc, Z., Celik, M., Onal, M., Sarikaya, Y., Oner, Y. & Acik, L. 2014 Study on the synthesis and properties of polyacrylamide/Na-montmorillonite nanocomposites. *Journal of Composite Materials* **48** (4), 439–446.

Kumar, K. V. 2006 Linear and non-linear regression analysis for the sorption kinetics of methylene blue onto activated carbon. *Journal of Hazardous Materials* **B137**, 1538–1544.

Kumar, D., Singh, A. & Gaur, J. 2011 Mono-component versus binary isotherm models for Cu(II) and Pb(II) sorption from binary metal solution by the green alga Pithophora oedogonia. *Bioresource Technology* **99**, 8280–8287.

Li, G., Qin, F., Yang, H., Lu, Z., Sun, H. & Chen, R. 2012 Facile microwave synthesis of 3D flowerlike BiOBr nanostructures and their excellent Cr^{VI} removal capacity. *European Journal of Inorganic Chemistry* **12**, 2508–2513.

Li, G., Qin, F., Wang, R., Shengqiang, X., Sun, H. & Chen, R. 2013 BiOX (X = Cl, Br, I) nanostructures: mannitol-mediated microwave synthesis, visible light photocatalytic performance, and Cr(VI) removal capacity. *Journal of Colloid and Interface Science* **409**, 43–51.

Liu, E., Zhao, H., Li, H., Li, G., Liu, Y. & Chen, R. 2014 Hydrothermal synthesis of porous ą-Fe_2O_3 nanostructures for highly efficient Cr(IV) removal. *New Journal of Chemistry* **38**, 2911.

Lopičić, Z. R., Stojanović, M. D., Marković, S. B., Milojković, J. V., Mihajlović, M. L., Radoičić, T. S. & Kijevčanin, M. L. 2016 Effects of different mechanical treatments on structural changes of lignocellulosic waste biomass and subsequent Cu(II) removal kinetics. *Arabian Journal of Chemistry.* Doi: http://dx.doi.org/10.1016/j.arabjc.2016.04.005, 1–13.

Lukman, S., Essa, M., Mu'azu, N., Bukhari, A. & Basheer, C. 2013 Adsorption and desorption of heavy metals onto natural clay material: influence of initial pH. *Journal of Environmental Science and Technology* **6** (1), 1–15.

Malamis, S. & Katsou, E. 2013 A review on zinc and nickel adsorption on natural and modified zeolite, bentonite and vermiculite: examination of process parameters, kinetics and isotherms. *Journal of Hazardous Materials* **252–253**, 428–461.

Maschio, G., Koufopanos, C. & Lucchesi, A. 1992 Pyrolysis, a promising route for biomass utilization. *Bioresource Technology* **42**, 219–231.

Moore, M. 2016 *Michael Moore, [blog] 10 things they won't tell you about the Flint tragedy. But I will*. Available from: http://michaelmoore.com/10FactsOnFlint/ (accessed 18 May 2016).

Nachtegaal, M., Scheidegger, A., Dähn, R., Chateigner, D. & Furrer, G. 2005 Immobilization of Ni by Al-modified montmorillonite: a novel uptake mechanism. *Geochimica et Cosmochimica Acta* **69**, 4211–4225.

Nicolaidis, S. 1998 Physiology of thirst. In: *Hydration throughout Life* (M. J. Arnaud, ed.). Eurotext, Montrouge, pp. 3–9.

Qin, F., Li, G., Wang, R., Wu, J., Sun, H. & Chen, R. 2012a Template-free fabrication of Bi_2O_3 and $(BiO)_2$ CO_3 nanotubes and their application in water treatment. *Chemistry: A European Journal* **18**, 16491–16497.

Qin, F., Li, G., Xiao, H., Lu, Z., Sun, H. & Chen, R. 2012b Large scale synthesis of bismuth hollow nanospheres for highly efficient Cr(IV) removal. *Dalton Transitions* **41**, 11263.

Sun, X., Xu, F., Sun, R., Fowler, P. & Baird, M. 2005 Characteristics of degraded cellulose obtained from steam-exploded wheat straw. *Carbohydrate Research* **340**, 97–106.

Torab-Mostaedi, M., Asadollahzadeh, M., Hemmati, A. & Khosravi, A. 2013 Equilibrium, kinetic, and thermodynamic studies for biosorption of cadmium and nickel on grapefruit peel. *Journal of the Taiwan Institute of Chemical Engineers* **44** (2), 295–302.

Tyagi, B., Chudasama, C. & Jasra, R. 2006 Determination of structural modification in deactivated montmorillonite clay by FT-IR spectroscopy. *Spectrochimica Acta Part A: Molecular and Biomolecular Spectroscopy* **64**, 273–278.

Wang, L., Wang, N., Zhu, L., Yu, H. & Tang, H. 2008 Photocatalytic reduction of Cr(VI) over different TiO_2 photocatalysts and the effects of dissolved organic species. *Journal of Hazardous Materials* **152**, 93–99.

Wysokowski, M., Klapiszewski, L., Moszyński, D., Bartczak, P., Szatkowski, T., Majchrzak, I., Siwińska-Stefańska, K., Bazhenov, V. & Jesionowski, T. 2014 Modification of chitin with kraft lignin and development of new biosorbents for removal of cadmium(II) and nickel(II) ions. *Marine Drugs* **12**, 2245–2268.

Xi, Y., Zhou, Q., Frost, R. & He, H. 2007 Thermal stability of octadecyltrimethylammonium bromide modified montmorillonite organoclay. *Journal of Colloid and Interface Science* **311**, 347–353.

Yuan, G., Theng, B., Churchman, G. & Gates, W. 2013 *Handbook of Clay Science, Part A, 2nd Edition: Clays and Clay Minerals for Pollution Control.* Elsevier, Amsterdam, pp. 587–644.

Zaarei, D., Sarabi, A., Sharif, F. & Kassiriha, S. 2008 Structure, properties and corrosion resistivity of polymeric nanocomposite coatings based on layered silicates. *Journal of Coatings Technology and Research* **5** (2), 241–249.

Zhang, X. & Wang, X. 2015 Adsorption and desorption of nickel (II) ions from aqueous solution by a lignocellulose/montmorillonite nanocomposite. *PLoS ONE* **10** (2), e0117077. doi:10.1371/journal.pone.0117077.

Zhou, G., Luo, J., Liu, C., Chu, L., Ma, J., Tang, Y., Zeng, Z. & Luo, S. 2016 A highly efficient polyampholyte hydrogel sorbent based fixed-bed process for heavy metal removal in actual industrial effluent. *Water Research* **89**, 151–160.

First received 13 November 2016; accepted in revised form 15 February 2017. Available online 1 March 2017